

# Making it Count: Quantitative MRI

## 19.1 Introduction

Ever since the earliest days of NMR and MRI the possibility of using quantitative measurements of NMR parameters has been proposed as a way of characterizing tissues and distinguishing pathologies. Apart from the obvious ones ( $T_1$  and  $T_2$  relaxation times), researchers have invested huge efforts to quantify blood velocity and flow, apparent diffusion coefficient (ADC), brain perfusion, fat content and tumour permeability. In addition MR is used to quantify some parameters indirectly, e.g. iron concentration (via  $T_2$  or  $T_2^*$ ), and cardiac functional parameters such as ejection fraction (via volumetric measurements). Unfortunately many of these techniques have not made the transition from research to daily clinical use, mainly because results for pathological tissue are not sufficiently different from those for normal tissue, or specific to a particular pathology. In this chapter we will show that:

- relaxation times can be measured in vivo with fairly good accuracy (if you pick the right technique);
- ADC can be measured but we need a more sophisticated model to achieve good accuracy;
- brain perfusion can be quantified in two ways, one of which may be accurate enough for clinical use;
- fat content of the liver is emerging as an important quantitative application;
- all quantitative methods suffer from systematic errors due to the imaging process;
- it is not enough to find a significant difference between healthy and disease groups; you have to pay attention to the statistics to know if a new technique will really change the MRI world.

## 19.2 Relaxation Times

### 19.2.1 $T_1$ Relaxation Time

A gold-standard  $T_1$  measurement is a rather time-consuming process if you want to avoid compromises.

A series of inversion recovery sequences is used with varying TI. After the initial inversion pulse, there is  $T_1$  recovery during the time TI. When the  $90^\circ$  is applied some of the tissue signals may still be negative (Figure 19.1c). In conventional MR imaging we usually generate the magnitude images, converting all negative signals to positive, which gives the IR curves shown in Figure 3.11. However, for  $T_1$  measurement it is better to use a 'real' reconstruction to make the post-processing easier. The signal at each TI is given by

$$S(TI) = M_0 \left[ 1 - 2\exp\left(-\frac{TI}{T_1}\right) + \exp\left(-\frac{TR - TI}{T_1}\right) \right]$$

Provided  $(TR - TI) > 5 \times T_1$ , we can ignore the second exponential term, and by plotting  $\ln(S_\infty - S(TI))$  against TI, we get a straight line with a slope equal to  $T_1$ . As a quick-and-dirty method, just plot  $S(TI)$  against TI and look for the crossing point where  $S(TI) = 0$ , and then estimate  $T_1 = \ln 2 \times TI$ .

The time-consuming part is that the delay between the  $90^\circ$  pulse and the next inversion pulse must always be at least five times the longest  $T_1$  present to relax (Figure 19.1d) (which presents a chicken-and-egg problem: you don't know what the  $T_1$  is until you've measured it, and if TR is too short you won't measure it correctly!). For in vivo scanning, these TRs prove very impractical. There are two alternative methods which are commonly used in clinical applications: the Look-Locker (LL) method, and Driven Equilibrium Single Pulse Observation of  $T_1$  (DESPOT<sub>1</sub>), which uses two gradient-echo scans with different flip angles to compute  $T_1$ .

The Look-Locker (LL) technique uses an initial inversion pulse followed by a series of low flip angle  $\alpha^\circ$  pulses (Figure 19.2). Each  $\alpha$  pulse tips  $M_z$  very slightly away from the  $z$  axis, giving a signal of  $M_z \sin \alpha$  in the transverse plane. As  $M_z$  relaxes from  $-M_0$  back to equilibrium, the  $\alpha^\circ$  pulses give a series of images

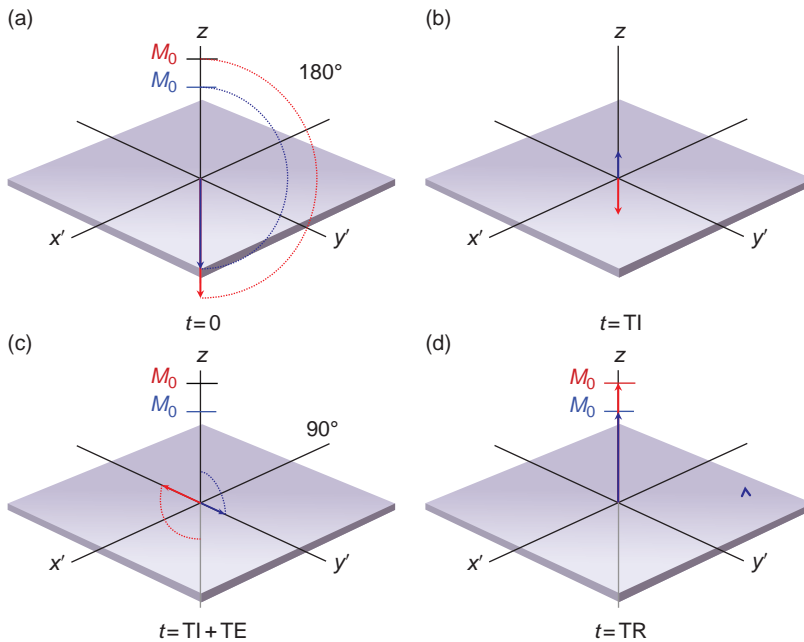


**Figure 19.1** (a) The initial  $180^\circ$  pulse inverts the magnetization, which then starts to recover. (b) When the  $90^\circ$  is applied some of the tissue signals may still be negative, so (c) a mixture of positive and negative echoes will be formed. The TR must always be at least five times the longest  $T_1$  present to allow full relaxation (d).

showing the changing magnetization. The main compromise with LL imaging is in the choice of the  $\alpha^\circ$  flip angle. If it is too small, the noise floor will dominate and SNR will be too low for reliable measurements. However if  $\alpha^\circ$  is too large, it will interfere with the true relaxation curve, accelerating the recovery towards  $+M_0$  and leading to underestimation of the true  $T_1$ . LL relaxometry lends itself to low-resolution fast imaging, in particular breath-hold cardiac  $T_1$  mapping (see Box ‘A Light Heart? Cardiac  $T_1$  Relaxometry’).

When high resolution is more important than speed, the DESPOT<sub>1</sub> method is a better choice. DESPOT<sub>1</sub> uses two (or more) spoiled gradient echo 3D sequences with different flip angles, keeping the same TR and TE for all the scans. From the signal equation for spoiled gradient echo, we can derive a linear relationship so that when we fit the data to a straight line, we can calculate  $T_1$  from the gradient of the fitted line (see Box ‘Drawing the Line: Plotting Graphs for  $T_1$  Relaxometry’). In practice, the choice of flip angles is critical and depends upon the TR chosen. In commercial versions of this method, it is common to be asked to enter a ‘target’  $T_1$ . DESPOT<sub>1</sub> is commonly used for quantitative dynamic contrast enhancement (DCE) imaging (see Section 19.4).

As with all imaging techniques, there are unavoidable errors which mean that  $T_1$  mapping can never be

perfect. For example, slice profiles are not perfect, giving a range of flip angles across the slice;  $B_1$  or  $B_0$  non-uniformities may have an impact on the signal; partial volume effects make it difficult to isolate single tissues. In spite of these problems – or rather by being aware of them and taking steps to minimize them –  $T_1$  relaxometry can achieve fairly good accuracy and precision.

#### Drawing the Line: Plotting Graphs for $T_1$ Relaxometry

In the LL technique, the apparent  $T_1$  (denoted  $T_1^*$ ) is found as usual by fitting the data to an exponential recovery curve. We can then use the following relationship to correct  $T_1^*$  and find the true  $T_1$ :

$$T_1 = T_1^* / \left[ \frac{1}{\cos \alpha} - 1 \right]$$

The DESPOT<sub>1</sub> method requires a bit more maths to see the linear relationship. We start with the signal equation for spoiled gradient echo, which can be written as

$$S(\alpha) = \frac{M_0(1 - E_1) \sin \alpha}{1 - E_1 \cos \alpha}$$

where  $E_1 = \exp(-TR/T_1)$  and we have assumed a  $TE \ll T_2^*$ . This can be rearranged as

$$\frac{S(\alpha)}{\sin \alpha} = E_1 \frac{S(\alpha)}{\tan \alpha} + M_0(1 - E_1)$$

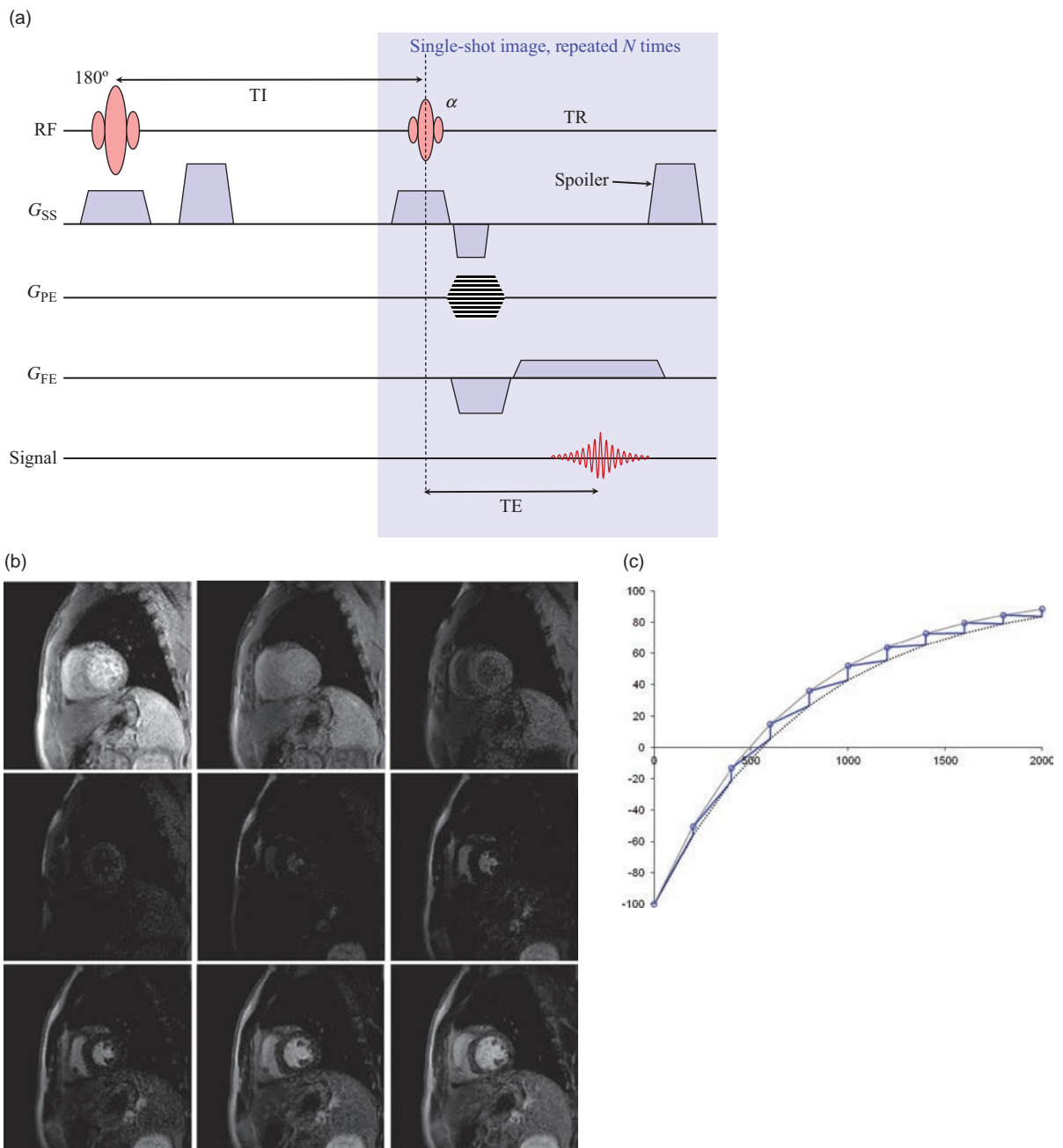


**Figure 19.2** (a) Look-Locker pulse sequence. (b) Series of images of the heart using a LL sequence. (c)  $M_z$  recovery curve in the LL technique (blue line). Blue circles indicate the measurement points at each  $\alpha$  flip angle. Note that the relaxation time  $T_1^*$  appears to be shorter (solid grey line) than the true  $T_1$  (dotted black line).

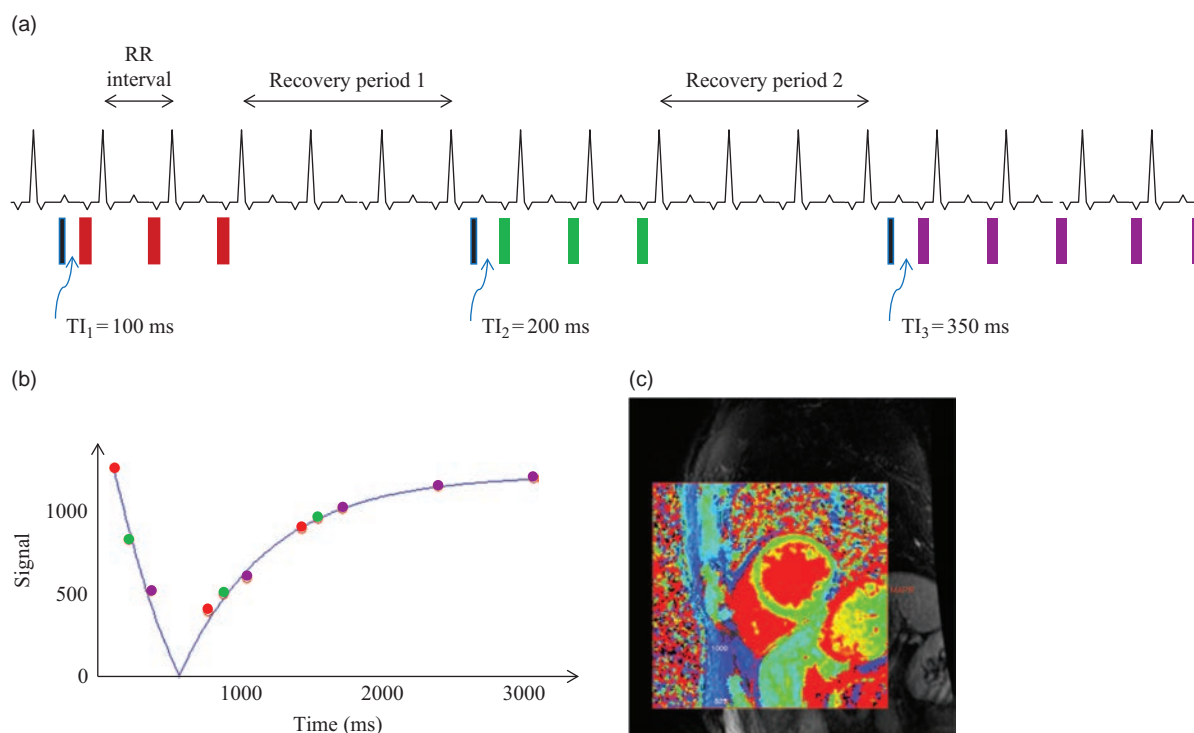


**Figure 19.3** (a) Modified Look-Locker Imaging (MOLLI) with a 3(3)3(3)5 scheme. Blue bars are inversion pulses, red bars are bSSFP images with a excitation pulses. See text for other details. (b) The relationship of the bSSFP acquisitions to the  $T_1$  recovery curve; purple points, first inversion set; green dots, second inversion set; orange dots, third inversion set. A magnitude inversion recovery model is fitted to the data points to determine the  $T_1$ , yielding (c) a  $T_1$  map.

which is a straight line of the form  $y = mx + c$ . We plot  $S(a)/\sin a$  against  $S(a)/\tan a$ , and fit a straight line to the data. The slope  $m$  of the plot is equal to  $E_1$ , from which we can obtain  $T_1$ :

$$T_1 = -\frac{TR}{\ln(m)}$$

### A Light Heart? Cardiac $T_1$ Relaxometry

Conventional imaging methods are excellent for detecting focal defects in the heart and great vessels, but systemic myocardial disease is harder to detect.  $T_1$  relaxometry is proposed as a bio-marker for diffuse cardiac fibrosis, myocarditis and other diseases. Apart from measuring the myocardial  $T_1$  directly (so-called 'native  $T_1$  mapping'),  $T_1$  measurements can also be used to estimate the extracellular volume (ECV) of fluid in the myocardium, as we will see at the end of this box. At the time of writing, it is unclear whether native  $T_1$  or ECV measurements will be the most useful in diffuse cardiopathies.

The Look-Locker method is the basis for quantitative  $T_1$  measurements in the myocardium, using an ECG-triggered variant known as MOLLI (**MODified Look-Locker Imaging**). MOLLI uses single-shot bSSFP readouts after each of the low flip angle  $\alpha$  pulses, and is of course fast enough to be done in a breath-hold. There are several ways to organize the bSSFP readouts between heartbeats, to allow for measuring the  $T_1$  recovery curve properly. The original MOLLI implementation has three inversion pulses and 11 readouts distributed over 17 heartbeats, as shown in Figure 19.3a. The first inversion pulse is followed by bSSFP readouts in the first three heartbeats, giving three inversion times of  $TI_1$ ,  $TI_1 + RR$  and  $TI_1 + 2 \times RR$ . The next three heartbeats are empty, to allow full relaxation. Another inversion pulse is applied followed by three more bSSFP readouts, providing three more inversion times at  $TI_2$ ,  $TI_2 + RR$  and  $TI_2 + 2 \times RR$ . After another three-beat relaxation period, the final inversion pulse is applied followed by five bSSFP readouts, giving a total of 11 inversion times. This scheme is called either MOLLI 3-3-5 or 3(3)3(3)5.

When the 11 images are placed in the correct T1 order, the apparent  $T_1^*$  and then the 'true'  $T_1$  can be calculated on a pixel-by-pixel basis.

There have been shorter MOLLI variants proposed, the most common of which is **Shortened** MOLLI (ShMOLLI) involving a 5(1)1(1)(1) acquisition. However, the data processing is more involved and is conditional upon the heart rate. All cardiac quantitative  $T_1$  techniques may require motion correction/registration of the individual images to improve accuracy.

To extend from measuring the native  $T_1$  to estimating the ECV,  $T_1$  mapping is performed at two time-points: one before a bolus injection of Gd, and the second approximately 15 min after the bolus injection. The relaxation rate is measured in the myocardium and in the blood-pool, and the ECV is then estimated as follows:

$$ECV = (1 - Hct) \cdot \frac{\Delta R_{1,myo}}{\Delta R_{1,blood}}$$

where  $Hct$  is the haematocrit,  $R_1 = 1/T_1$  and  $\Delta R_1$  is the change in  $R_1$  at the pre- and post-Gd time-points. Literature values for  $Hct$  can be used (0.45 for men and 0.40 for women), but it is preferable to take the patient's true  $Hct$  value since this also varies with disease. The normalization by the blood-pool  $T_1$  is necessary to avoid confounding factors such as Gd clearance rate. The typical ECV of normal myocardium has been shown to be around 20–30%.

## 19.2.2 $T_2$ and $T_2^*$ Relaxation Times

To measure  $T_2$ , you might intuitively use a series of spin-echo sequences and measure the signal height at each TE. Plotting a graph of signal against TE would show an exponential decay and allow us to find  $T_2$ . Unfortunately we can't use separate scans: the diffusion of protons through an inhomogeneous magnetic field adds an irreversible dephasing which reduces the signal much faster than the true  $T_2$ . It's also very inefficient, since we can acquire several echoes after each  $90^\circ$  pulse. Back in the 1950s it was shown that a series of equally spaced  $180^\circ$  pulses on the  $+x'$  axis creates a train of spin echoes alternating between negative and positive signs. This is known as a Carr–Purcell echo train, and the signal at time  $t$  is given by

$$S(t) = M_0 \left[ \exp\left(\frac{-t}{T_2}\right) \cdot \exp\left(\frac{-2\gamma^2 \Delta B^2 D \tau^2 t}{3}\right) \right]$$

where  $\Delta B$  is the magnetic field inhomogeneity,  $2\tau$  is the echo spacing,  $D$  is the diffusion coefficient and  $t$  is the overall time from the excitation to a particular echo we are measuring. Provided the echo spacing is small, the second term is almost equal to 1, and we are left with an exponential decay due to  $T_2$ . A further modification known as the Carr–Purcell–Meiboom–Gill (CPMG) sequence compensates for imperfections in the  $180^\circ$  echo which would otherwise accumulate over the echo train. In CPMG, the initial  $90^\circ$  pulse is on the  $+x'$  axis, the train of  $180^\circ$  pulses is on the  $+y'$

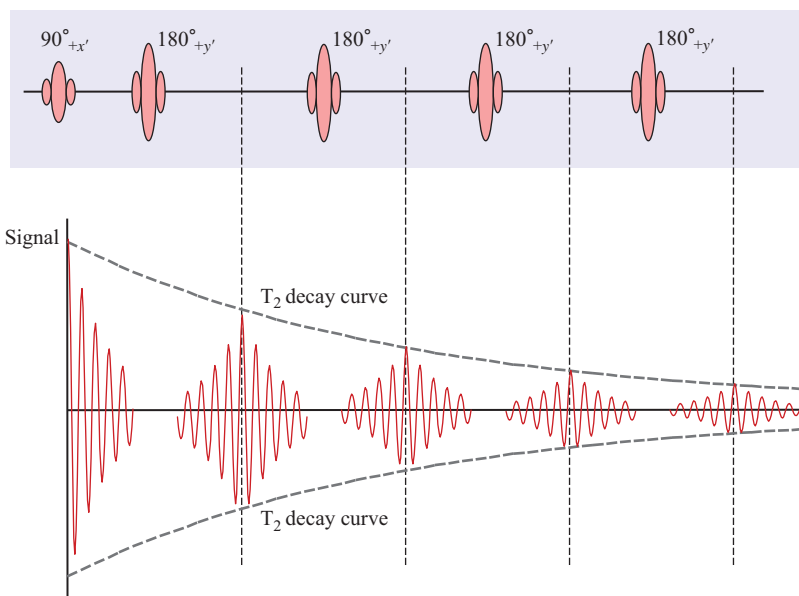


**Figure 19.4** The Carr–Purcell–Meiboom–Gill sequence showing four echoes.

axis and all the echoes are positive (Figure 19.4). If the 180° pulse is imperfect, the first and every odd-numbered echo will be slightly too small, but the even echoes will be the correct height, and the errors do not accumulate. To measure  $T_2$ , we should therefore use the echo height from only the even echoes. At least five echo heights should be used (implying an echo train of at least ten) with a range of echo times up to about three times  $T_2$ .

For in vivo relaxometry, we need to make sure the TR is long enough for complete  $T_1$  relaxation between the 90° pulses. The  $T_2$  scan must be a classic SE sequence – we cannot use the echo train for phase encoding – and the rather long echo train puts limits on the number of slices that can be acquired. Scan times are typically 8–10 min, which is reasonable. An alternative method for  $T_2$  relaxometry is called Driven Equilibrium Single Pulse Observation of  $T_2$  (DESPOT<sub>2</sub>), which uses a series of 3D fully rewound gradient-echo scans with different flip angles  $\alpha$ . See Box ‘Big Brother is Measuring  $T_2$ ’ for more details.

Measuring  $T_2^*$  is almost identical to measuring  $T_2$ , except that we use a multi-echo gradient-echo scan. We simply fit the multi-echo signal heights to a mono-exponential decay curve to derive  $T_2^*$ :

$$S(t) = M_0 \exp\left(\frac{-t}{T_2^*}\right).$$

However, there are some critical issues about measuring  $T_2^*$ , related to the main field inhomogeneity. Since all modern scanners perform automatic shimming per patient, often with no way for the user to control the process, it is difficult to know if changes in  $T_2^*$  are due to changes in the tissue itself, or independent changes in  $\Delta B_0$ . Accuracy and precision are particularly influenced by  $\Delta B_0$ , especially if comparing between different field strengths. Finally, there is no real ‘gold’ standard to use as a reference measure.

As with  $T_1$  relaxometry,  $T_2$  and  $T_2^*$  relaxometry methods suffer from problems related to the imaging method, in particular flip angle variations across the slice profile and  $B_1$  inhomogeneity effects.

#### Big Brother is Measuring $T_2$

The signal equation for DESPOT<sub>2</sub> is based on the equation for fully rewound gradient echo:

$$S(\alpha) = \frac{M_0(1 - E_1) \sin \alpha}{1 - E_1 E_2 - (E_1 - E_2) \cos \alpha}$$

where  $E_1 = \exp(-TR/T_1)$  and  $E_2 = \exp(-TE/T_2)$ . As before, this can be recast as a linear equation:

$$\frac{S(\alpha)}{\sin \alpha} = \frac{E_1 - E_2}{E_1 E_2} \cdot \frac{S(\alpha)}{\tan \alpha} + \frac{M_0(1 - E_1)}{E_1 E_2}$$

$T_2$  can be found from the gradient  $m$  of a plot of  $S(\alpha)/\sin \alpha$  against  $S(\alpha)/\tan \alpha$ :

$$T_2 = -TR / \ln\left(\frac{m - E_1}{mE_1 - 1}\right)$$

Notice that it is necessary to know the tissue  $T_1$  in order to find the  $T_2$ . This limits the application of DESPOT<sub>2</sub> as a standalone sequence, so most often it is done in combination with DESPOT<sub>1</sub>.

Conceptually, once we know both  $T_1$  and  $T_2$  for all the tissues, we can use the signal equations to generate images with any contrast we desire. Over the years there has been intermittent interest in ‘synthetic’ imaging, but it has suffered from limitations; the signal equations generally do not include flow or diffusion effects, and cannot predict how Gd will affect the images. Recently this interest has resurfaced, based on a new magnetization-prepared SE acquisition method which compensates for non-uniformities in  $B_1$ . It has been commercialized by GE Healthcare under the name of MAGIC (MAGnetic resonance Image Compilation) and is also supported on Philips systems.

#### Too Many Irons in the Fire: Monitoring Iron Overload With MRI

Excess iron in the body is stored in the liver, in the form of ferritin or haemosiderin, and can also accumulate in the cardiac muscle. This occurs in patients with hereditary or idiopathic haemochromatosis, and those who have had repeated transfusions for chronic anaemias such as thalassaemia. Iron overload can lead to liver fibrosis, cirrhosis, hepatocellular carcinoma and heart or liver failure.

In the liver, either  $T_2$  or  $T_2^*$  relaxometry can be used to assess liver iron concentration. Empirically it has been shown that the iron load is correlated to the inverse of relaxation time, i.e. the relaxation rates  $R_2$  or  $R_2^*$ . The FerriScan method is a commercially available service which is FDA approved for measuring liver iron content. It uses motion-corrected  $R_2$  maps calculated from a series of single spin echoes and results are processed offline at FerriScan’s offices (Figure 19.5). It requires careful calibration of the scanner using a standard phantom. Other methods use  $R_2^*$  calculated from a multi-echo gradient-echo



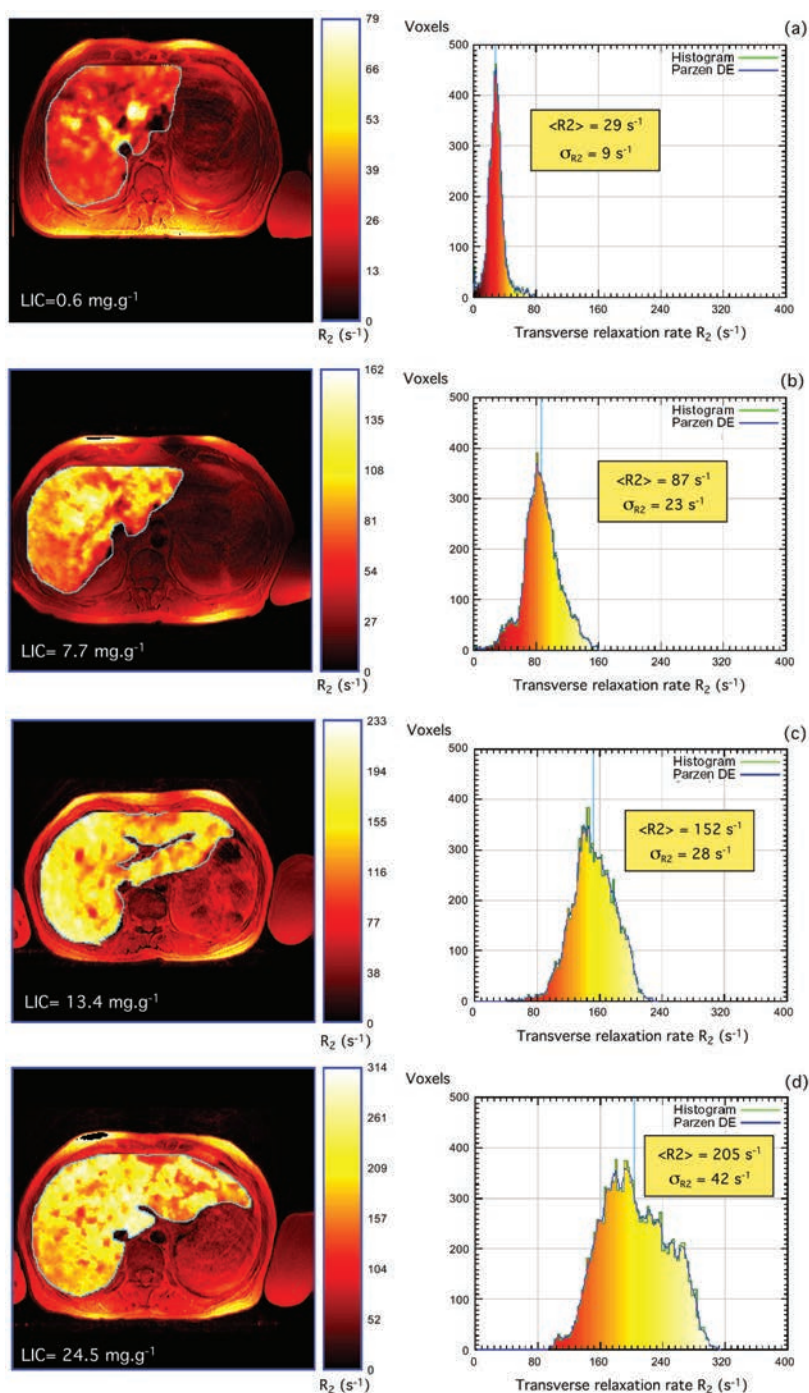


**Figure 19.5** R<sub>2</sub> maps and histograms demonstrating different levels of liver iron concentration: (a) healthy liver, (b) mild overload, (c) moderate overload, and (d) severe overload. Images courtesy of Resonance Health Ltd, providers of FerriScan R2-MRI [www.resonancehealth.com](http://www.resonancehealth.com)

sequence. However, care is required for there are scanner-specific errors (from  $\Delta B_0$ ), the measurement of high R<sub>2</sub><sup>\*</sup> (short T<sub>2</sub><sup>\*</sup>) is prone to errors due to very low SNR and there is no universal calibration. With careful measurement methods, a linear relationship

between iron content from liver biopsy results and R<sub>2</sub><sup>\*</sup> can be obtained.

In the heart, quantitative T<sub>2</sub><sup>\*</sup> measurement has been proposed to monitor progression of iron overload in these patient populations. An ECG-gated

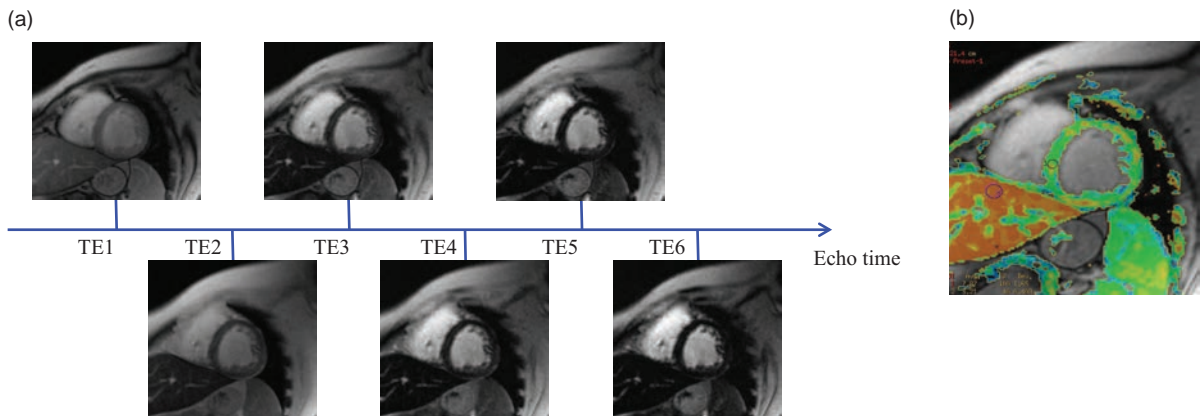


**Figure 19.6** (a) A series of cardiac images acquired at increasing TE. (b) Quantitative  $T_2^*$  data overlaid on an anatomical image. The myocardial ROI shows a  $T_2^*$  of 8 ms, while the liver ROI shows a  $T_2^*$  of 3 ms. These values are typical for a patient with iron overload.

breath-hold multi-echo gradient-echo imaging technique is used, followed by  $T_2^*$  calculation on a pixel-by-pixel basis. The choice of TEs is very important: in cases of severe iron overload, the  $T_2^*$  may be so short that the signal has decayed before the first echo is acquired. Conversely, in cases of low iron overload, selecting a range of TEs that are too short will only show the first part of the decay curve, reducing accuracy. The practical answer is to use the shortest possible echo spacing, but with at least five echoes. Various research studies have suggested that  $T_2^*$  values higher than 20 ms can be considered normal, while lower  $T_2^*$ s indicate iron loading (see Figure 19.6).

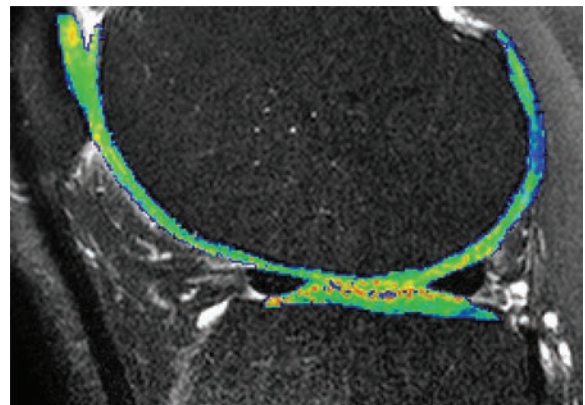


**Figure 19.7**  $T_2$  cartilage map.

### 19.2.3 Sources of Error in In Vivo Relaxometry

Apart from all these problems, there are still others which introduce significant errors in in vivo relaxometry. These include poor sequence parameter choice, particularly too short a TR for the PD-weighted image, inhomogeneous RF pulses, unwelcome magnetization transfer effects in multiple-slice acquisitions arising from selective (therefore off-resonance) pulses intended for other slices, and slice profile distortions. It is extremely important to understand these error sources, especially when trying to compare relaxometry results between different systems or in a multi-centre study.

#### Knee-Jerk Reactions: Cartilage Relaxometry

Osteo-arthritis (OA) is a chronic disease which results in degeneration of the joints and is a major cause of

pain and morbidity among the ageing population. It has been proposed that  $T_2$  relaxometry is a biomarker for cartilage degeneration.  $T_2$  is sensitive to changes in the collagen matrix, increasing significantly both locally and globally in osteoarthritic joints. In patients who have had transplanted chondrocytes, monitoring of  $T_2$  can identify cartilage repair (Figure 19.7).  $T_2$  cartilage measurements suffer from poor precision due to low SNR, noise floor bias (because we use magnitude reconstruction, giving a non-Gaussian noise distribution) and partial volume effects.

$T_1$  relaxometry is also useful in cartilage assessment. As a precursor to OA, glycosaminoglycan (GAG) molecules break down. Since both GAG molecules and gadolinium are negatively charged, gadolinium will penetrate articular cartilage in inverse proportion to the local GAG concentration.  $T_1$  quantification follows an injection of a Gd-based contrast



agent intravenously. After 30–90 min of exercise post-injection, the Gd penetrates the cartilage.  $T_1$  relaxometry will give an indication of GAG concentration and hence cartilage integrity. As GAG decreases, the Gd concentration increases and  $T_1$  decreases, so shorter  $T_1$ s indicate a more advanced disease process. This technique is often known as dGEMRIC (delayed Gadolinium-Enhanced MRI of Cartilage).

Other less common quantitative investigations of cartilage include  $T_{1\rho}$  (pronounced 'tee wun roh', sometimes written as  $T_1$ -rho) or sodium ( $^{23}\text{Na}$ ) imaging.  $T_{1\rho}$  refers to spin–lattice relaxation in the rotating frame, and requires specialist pulse sequences. Sodium has extremely short  $T_2$  in vivo, so ultra-short TE imaging sequences are required. Since the gyromagnetic ratio of  $^{23}\text{Na}$  is 11.27 MHz  $T^{-1}$ , special RF transmission and reception hardware and coils are also required.

### 19.3 Diffusion Parameters

The apparent diffusion coefficient ADC is routinely calculated in clinical practice, in order to separate true diffusion effects from  $T_2$  shine-through (see Section 18.2.2). Since tumours appear very bright on diffusion-weighted images, they obviously have reduced ADCs compared with normal tissue. Regions of interest on the ADC map can easily provide the ADC of various tissues. Numerous studies have been conducted using ADC in various cancers (breast, liver, prostate, brain, etc.); however, there is significant diversity in the results. It turns out that we need a better model of the diffusion process.

In practice, what we measure in normal DWI is related to the actual diffusion coefficient but also contains contributions from other sources of tissue

motion. Microcirculation in pseudo-random capillary systems is one such source of so-called IntraVoxel-Incoherent Motion (IVIM). Bulk flow and motion will also seriously degrade the measurements and lead to image artefacts.

An implicit assumption in the simple ADC calculation is that there is a single diffusion coefficient. By collecting multiple  $b$ -factor DW-images, it is possible to see that the signal decay is not mono-exponential, and in most organs it is in fact bi-exponential (Figure 19.8). The signals from the multi- $b$ -factor scan can be fitted to this two-compartment model, which is shown mathematically as

$$S(b) = S_0 \cdot \left[ f_{\text{perf}} \cdot \exp(-bD^*) + (1 - f_{\text{perf}}) \cdot \exp(-bD) \right]$$

where  $f_{\text{perf}}$  is the volume fraction of the perfusion compartment, which has pseudo-diffusion coefficient  $D^*$ .

This is known as the IVIM model, where the shorter diffusion coefficient is actually due to capillary perfusion, and only the longer one is due to true diffusion of water. These two compartments have different sizes, depending on the organ, but also depending on any pathology that may be present.

Bi-exponential fitting, especially when the sizes of the two compartments are not independent, is notoriously difficult. So even using the IVIM model, it proves tricky to achieve good accuracy and reproducibility of diffusion quantification. As a workaround, some researchers revert to the mono-exponential calculation, but using a low  $b$ -factor (e.g.  $b = 50$ – $100$ ) image instead of  $b = 0$  in the calculation of ADC:

$$D = \frac{\ln S(b_2) - \ln S(b_1)}{b_1 - b_2}$$

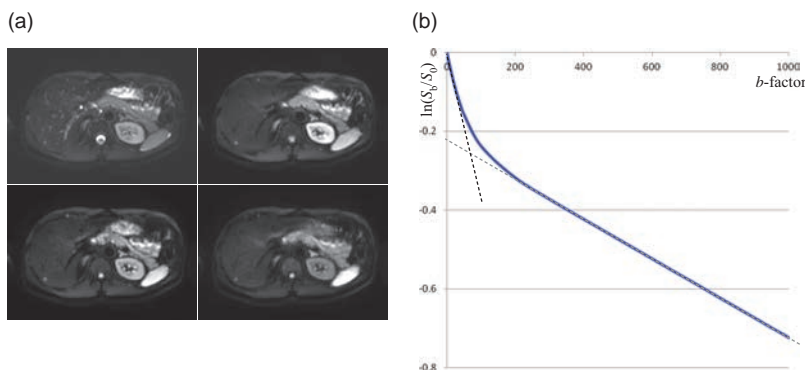


**Figure 19.8** (a) Series of DW images of the liver with various  $b$ -factors. (b) Plot of  $\ln(S_b/S_0)$  vs  $b$ -factor is bi-exponential, revealing two components: the true diffusion (dashed grey line) and the pseudo-diffusion, or perfusion fraction (dashed black line).

## 19.4 Tissue Perfusion and Permeability

Tissue perfusion, in particular for brain imaging, is important for vascular diseases like stroke and vascular dementia. Perfusion is the rate of blood flow per 100 g of tissue, and is critical to deliver sufficient oxygen and glucose to the cells. The average perfusion rate for the whole brain is  $50\text{--}55\text{ ml min}^{-1} 100\text{g}^{-1}$ , measured using PET. It is widely accepted that if perfusion falls below  $20\text{ ml min}^{-1} 100\text{g}^{-1}$  tissue ischaemia will start to cause damage to cells, and eventually cell death will occur if perfusion is lower than  $10\text{ ml min}^{-1} 100\text{g}^{-1}$ . Since these thresholds are well-established, quantification of perfusion is an important marker during the initial work-up of ischaemic stroke. Outside the brain, permeability is a more accessible parameter, particularly useful in cancer because most tumours have characteristically 'leaky' endothelial cells and an abundant capillary bed. So leaky, in fact, that many tumours show enhanced signal during the first pass of the Gd agent in the vascular system.

As we already saw in Chapter 18, there are two methods for measuring brain perfusion: first-pass Gd, also known as dynamic susceptibility contrast (DSC) imaging, and arterial spin labelling. Refer back to Box 'Advanced Processing and Quantification' to see how DSC data can be processed to derive the cerebral perfusion, and to Box 'ASL Analysis' for the ASL model processing. Chapter 18 also describes the processing to extract permeability parameters from dynamic contrast enhancement (DCE) imaging, in Box 'Mathematical Modelling: The MRI Catwalk'. Since these models seem fairly straightforward, you might be wondering why quantitative perfusion and permeability are not part of the clinical routine.

In the case of DSC perfusion and permeability, there is a significant problem measuring the arterial input function (AIF) in the in-flowing blood. Arterial flow is typically very fast, so we need extremely high temporal resolution to capture the true shape of the Gd bolus as it passes – usually far higher than we can achieve in practice. The model also assumes a linear relationship between Gd concentration and blood signal, which is (probably) not valid at high concentrations such as the bolus peak. So we can assume that the AIF is underestimated, but we have no idea by how much. Some research groups have used calibration factors, e.g. comparing normal volunteers with DSC-perfusion and PET, to improve quantification, but this is unreliable in any pathological condition

where the arterial flow is different from normal. In DCE, there are attempts to use 'model' or population-averaged AIFs in the processing: even though this gives better results than trying to estimate the AIF each time, inevitably there will be unpredictable changes in some disease conditions.

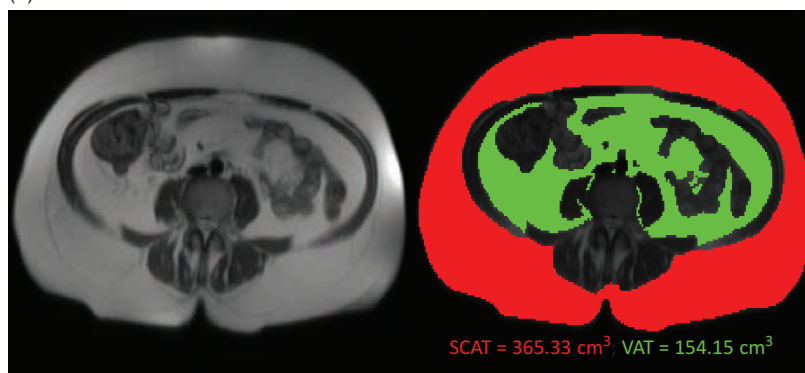
That leaves ASL. Indeed this method is still considered 'promising' for quantification of brain perfusion, and researchers are starting to use it in other organs too. Many of the key difficulties can be overcome by careful tuning of the magnetic labelling pulses (adapting the pulse sequence) and by including exchange times in the model. ASL in the brain shows better accuracy and reproducibility than DSC perfusion, and is also showing good results when inter-site comparisons are made. It is too early to say that it 'works', but it is currently the favourite horse in this particular race.

## 19.5 Fat Quantification

The current obesity epidemic has led to considerable interest in methods for the quantification of fat as a marker of disease progression or to monitor therapeutic interventions. It has been shown that people with high abdominal visceral adiposity, sometimes referred to as the TOFI (Thin on the Outside, Fat on the Inside) phenotype, are at a substantially higher risk of developing so-called metabolic syndromes including type II diabetes and cardiovascular disease. MRI is an ideal modality for measuring SubCutaneous Adipose Tissue (SCAT) and Visceral Adipose Tissue (VAT), typically using a fast gradient-echo  $T_1$ w sequence with good contrast between fat and other tissues. Quantification of SCAT and VAT then becomes an image analysis task, and there are several software tools available which calculate the volumes. Figure 19.9 shows a single-slice  $T_1$ w image that has been semi-automatically segmented into SCAT and VAT. Dixon techniques are now offering a good alternative to  $T_1$ w imaging.

The quantification of intra-organ fat, such as in the liver, is a little more complex since large vacuoles of triglyceride fat accumulate in the liver cells in a process known as steatosis. Since alcohol may also contribute to the disease, fatty liver is often categorized as either alcoholic or Non-Alcoholic Fatty Liver Disease (NAFLD). If inflammation is also present, then this is referred to as alcoholic steatohepatitis or Non-Alcoholic SteatoHepatitis (NASH). Measurement of liver fat fraction is becoming very important

(a)



(b)

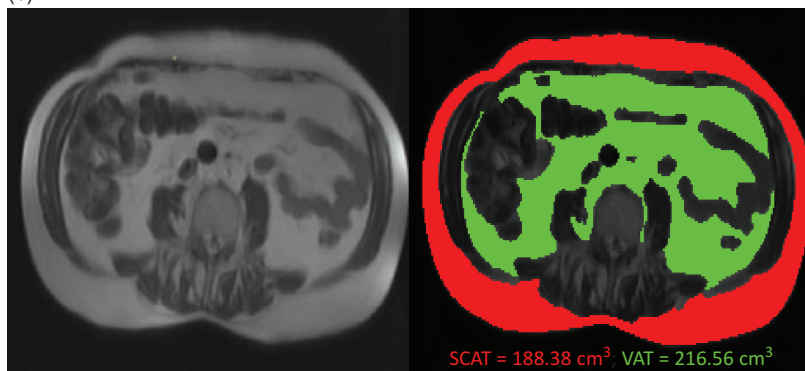


**Figure 19.9** Measurement of subcutaneous adipose tissue (SCAT) and visceral adipose tissue (VAT) from two different subjects. (a) A subject with a large subcutaneous fat deposit. (b) A subject with the TOFI (thin on the outside fat on the inside) phenotype.

in the Western world as researchers investigate these 'lifestyle' diseases and potential therapies for them.

For the liver, it is simple to calculate a hepatic fat fraction (HFF) from a gradient-echo Dixon scan, using the signal in the magnitude water and fat images as follows:

$$\text{HFF} = \frac{|S_f|}{|S_f| + |S_w|}$$

However, this simple approach ignores several confounding effects. Remember that gradient-echo Dixon scans have at least two echoes, and often five or more. Clearly, the first echo is acquired at a different TE to the second or later echoes, so we have to take into account the effect of  $T_2^*$  in the signal model. We typically estimate  $T_2^*$  using a multi-echo acquisition, i.e. a scan with five or six echoes. This is particularly important in patients with high iron concentration in the liver, a condition which occurs in about 40% of patients with steatosis. Second,  $T_1$  relaxation may also cause inaccuracies in the HFF measurement and fat-quantification scans use a low

flip angle, e.g. 5°. Although a small residual  $T_1$  bias may exist, this can be corrected using literature values for the  $T_1$  of fat and liver. Finally, accurate HFF measurements require a more sophisticated signal model with six or seven fat peaks, rather than just a single methylene peak (Figure 19.10). Commercial software packages provide not only the HFF maps (see Box 'Swapping Notes: More Detail about Dixon Reconstruction'), but also  $T_2^*$  or  $R_2^*$  maps (see Figure 19.11). Clinically  $R_2^*$  maps are useful because shorter  $T_2^*$  values, that are usually associated with pathology, appear brighter.

#### Swapping Notes: More Detail About Dixon Reconstruction

The in-phase echo ( $S_{IP}$ ) is the sum of water ( $S_w$ ) and fat ( $S_f$ ) signals, while the out-of-phase echo ( $S_{OP}$ ) is the difference:

$$\begin{aligned} S_{IP} &= (S_w + S_f) \cdot \exp(i\phi_0) \\ S_{OP} &= (S_w - S_f) \cdot \exp(i\phi_0) \cdot \exp(i\phi) \end{aligned}$$

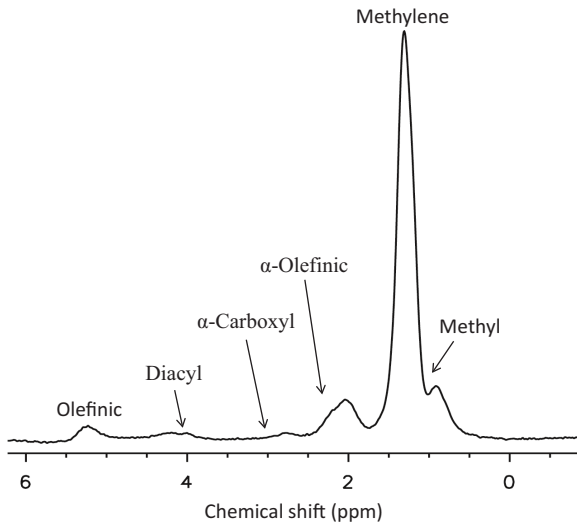


**Figure 19.10** Water-suppressed spectrum of human subcutaneous fat, showing six different proton resonances. Courtesy of Dr Mary McLean, University of Cambridge, UK.

The term  $\exp(i\phi)$  represents the phase shift, due to  $B_0$  non-uniformity ( $\Delta B_0$ ), accumulated during the echo shift  $\tau$ , i.e. it only applies to the out-of-phase image.

$$\phi = \gamma \Delta B_0 \tau$$

The term  $\exp(i\phi_0)$  represents all other phase errors that are the same for both images. Ignoring the phase shifts and simply adding the two images would result in a water-only image, while subtracting the OP image from the IP image leaves a fat-only image:

$$S_{IP} + S_{OP} = (S_w + S_f) + (S_w - S_f) = 2S_w$$

$$S_{IP} - S_{OP} = (S_w + S_f) - (S_w - S_f) = 2S_f$$

This is the so-called two-point Dixon (2PD) technique and is often referred to as a  $\{0, \pi\}$  technique reflecting the fact that there is a 0 and  $\pi$  (180°) phase shift between the two acquisitions. The main problem with this technique is that the assumption of zero background phase shifts ( $\exp(i\phi) = 1$ ) is not valid in practice. Dixon originally attempted to circumvent this problem by dealing only with magnitude images, which ignore the phase of the signal:

$$S_w = 0.5 \times (|S_{IP}| + |S_{OP}|) \quad S_f = 0.5 \times (|S_{IP}| - |S_{OP}|)$$

However, this calculation is only valid when the relative fraction of water in a voxel is greater than or equal to the fat fraction. If the situation is reversed,

i.e. the fat fraction is greater than the water fraction in the voxel, then the pixel values will be swapped. The following worked example demonstrates this effect. First consider a voxel which contains 60% water and 40% fat, then

$$S_{IP} = (S_w + S_f) = 0.6 + 0.4 = 1.0$$

$$S_{OP} = (S_w - S_f) = 0.6 - 0.4 = 0.2$$

Using the magnitudes of the signals, Dixon's reconstruction gives:

$$S_w = 0.5 \times (|1.0| + |0.2|) = 0.6$$

$$S_f = 0.5 \times (|1.0| - |0.2|) = 0.4$$

which is the correct answer. However, if the voxel contains 40% water and 60% fat, then

$$S_{IP} = (S_w + S_f) = 0.4 + 0.6 = 1.0$$

$$S_{OP} = (S_w - S_f) = 0.4 - 0.6 = -0.2$$

This time Dixon's method gives

$$S_w = 0.5 \times (|1.0| + |-0.2|) = 0.6$$

$$S_f = 0.5 \times (|1.0| - |-0.2|) = 0.4$$

which is wrong! The water image is allocated the fat fraction and the fat image the water fraction, i.e. the pixel is misclassified as being predominantly water and not fat. The Dixon reconstruction algorithms attempt to ensure that this error does not occur but sometimes, particularly in areas of large phase shift such as the dome of the liver, water-fat swaps can occur. Figure 19.12 shows an example of a Dixon water-fat swap artefact.

The difficulty with not knowing the background phase shifts led to the development of three-point Dixon (3PD) techniques where three separate acquisitions are performed, each with different echo shifts  $\tau$ , resulting in  $\{0, \pi, 2\pi\}$  phase shifts. The 0 and  $2\pi$  acquisitions, in which water and fat are both in-phase, can then be used to calculate  $\exp(i\phi)$ . We now have three equations:

$$S_0 = (S_w + S_f) \cdot \exp(i\phi_0)$$

$$S_\pi = (S_w - S_f) \cdot \exp(i\phi_0) \cdot \exp(i\phi)$$

$$S_{2\pi} = (S_w - S_f) \cdot \exp(i\phi_0) \cdot \exp(i2\phi)$$

We can then calculate  $\phi$  from

$$\hat{\phi} = 0.5 \cdot \tan^{-1}(S_0 \cdot S_{2\pi}^*)$$

where  $*$  represents taking the complex conjugate. In this equation, we use the symbol  $\hat{\phi}$  rather than  $\phi$  because it is only possible to determine the result within the range  $-\pi$  to  $+\pi$ , i.e. any phase shift less



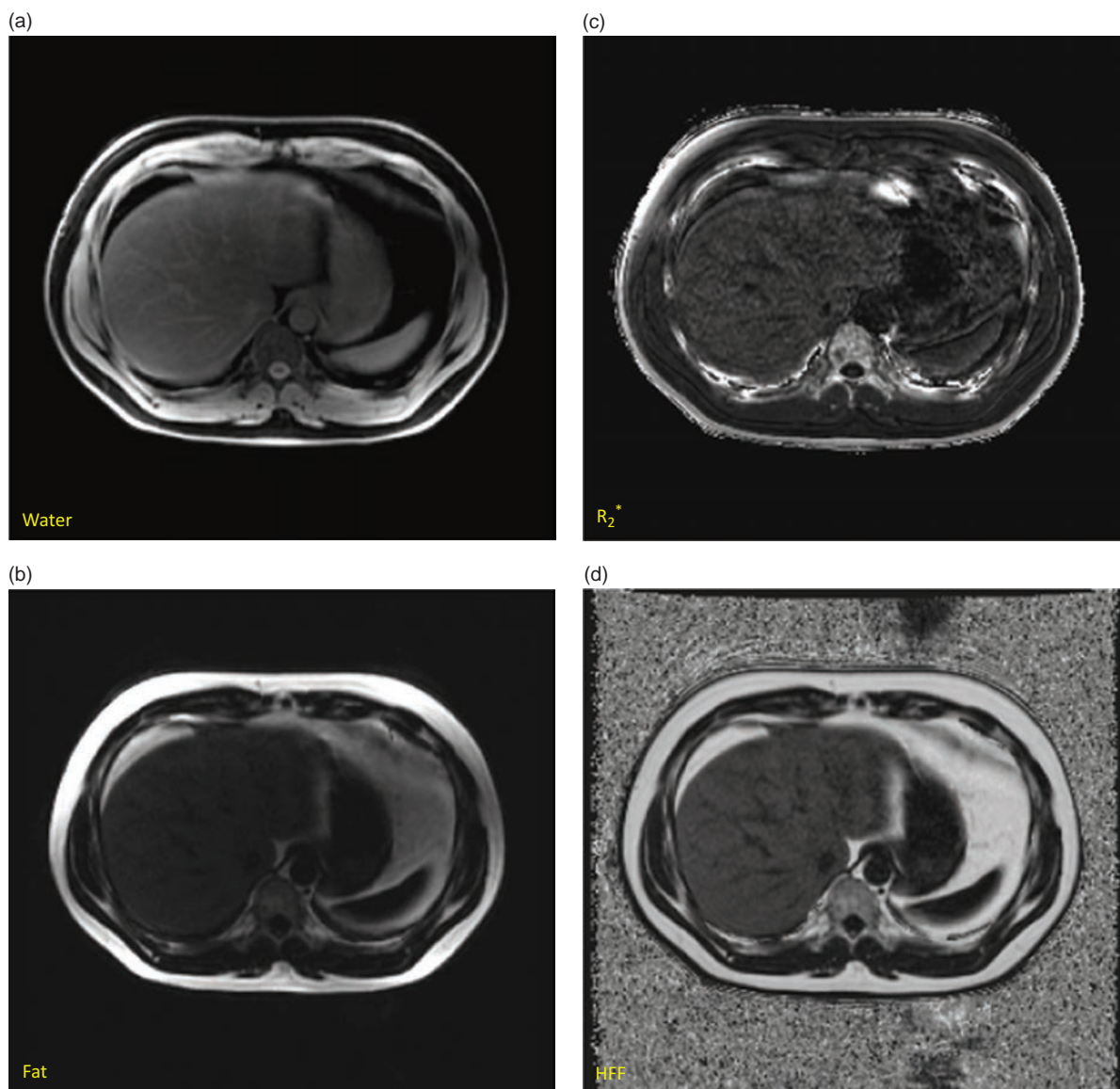


**Figure 19.11** Quantitative hepatic fat fraction (HFF) imaging using a six-echo gradient-echo acquisition obtained in a single breath-hold. (a) Water-only image. (b) Fat-only image. (c) Quantitative  $R_2^*$  map obtained by a pixel-by-pixel fit to the  $T_2^*$  exponential decay curve. (d) Quantitative HFF map. A region of interest in the liver measures approximately 20% HFF in this subject.

than  $-\pi$  or greater than  $\pi$  will have a multiple of  $2\pi$  added or subtracted to bring the phase back into the range  $-\pi$  to  $+\pi$ . This means that in the regions where the phase is wrapped, the signals from fat and water can be swapped. Fortunately, this problem of phase wrapping exists in many branches of physics and engineering and there is an extensive literature on phase-unwrapping algorithms that can be used to extract the correct sign of the signal.

## 19.6 MR Elastography

MR Elastography (MRE) is a method for quantitatively assessing the mechanical properties of tissue, primarily the tissue stiffness. For centuries, physicians have used palpation as a diagnostic method to determine an organ's size, shape, position and stiffness. The stiffness is particularly important since many disease conditions can increase the stiffness of an organ either



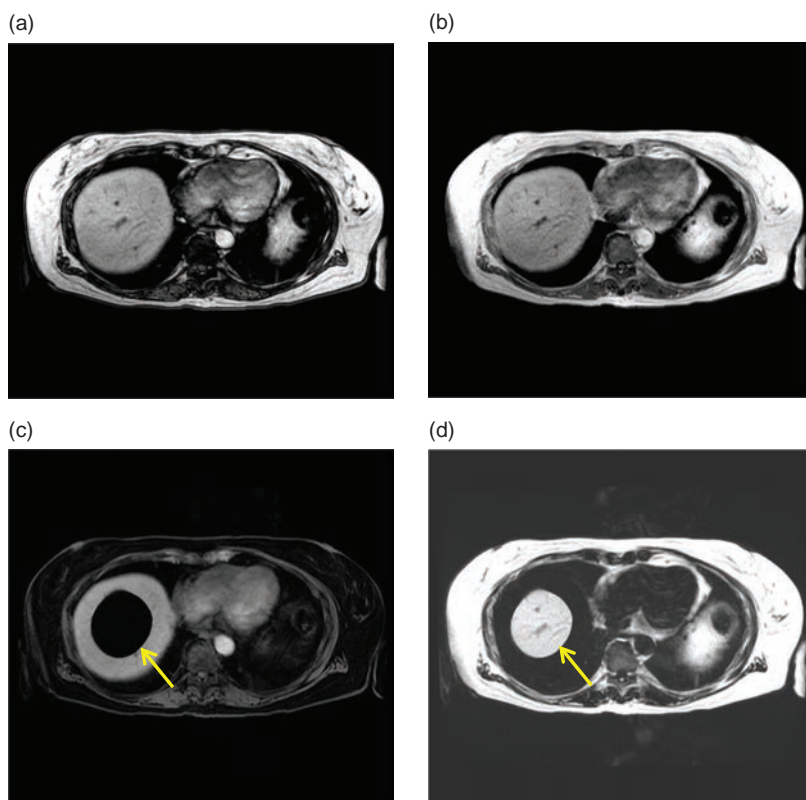


**Figure 19.12** Dixon water–fat swap artefact. The figure shows images from a dual-echo gradient-echo acquisition with the (a) first OP echo image acquired at TE = 2.3 ms and the (b) second IP echo image acquired at TE 4.6 ms. Following Dixon processing separate (c) water and (d) fat images are reconstructed, but in this case the Dixon reconstruction algorithm has incorrectly classified water and fat (arrows).

globally or focally, and the difference between normal and pathological tissues may be as high as five orders of magnitude. For example, fat has a shear modulus of  $10^2$  Pa while that of bone is more than  $10^7$  Pa. Creating non-invasive ‘maps’ of tissue stiffness may therefore offer some unique insights into disease characterization and therapeutic interventions.

MR elastography was first proposed in 1995 by Ehman’s research group at the Mayo Clinic. MRE uses an external driver system to create mechanical waves that propagate through the body, and generates quantitative images, known as elastograms, displaying the shear modulus of the tissue. Since 2012 this technology has been commercially available on conventional MRI systems, for the important clinical application of assessing hepatic fibrosis, a condition linked to alcohol-related disease and to obesity.

#### Stretch Your Imagination: Quantifying Elasticity

From school, you probably remember that the stiffness of a material is called the elastic modulus or Young’s modulus. Young’s modulus is the ratio of stress, i.e. the force per unit area applied to the

sample, to strain, i.e. the linear deformation of the sample. Conventionally given the symbol  $E$  (for elastic), the modulus is calculated from the equation

$$E = \frac{\text{stress}}{\text{strain}} = \frac{F/A_0}{\delta l/L_0},$$

where  $F$  is the force applied in the direction of  $L_0$ ,  $A_0$  is the cross-sectional area perpendicular to  $L_0$ , and  $\delta l$  is the deformation. As well as measuring Young’s modulus via a static experiment (like you did at school), it can also be measured by setting up a series of longitudinal waves in the material, and then measuring the speed  $c$  of the waves:

$$c = \sqrt{\frac{E}{\rho}} \Rightarrow E = \frac{(\lambda f)^2}{\rho}$$

where  $\rho$  represents the mechanical density of the material (instead of proton density), and  $\lambda$  and  $f$  are the wavelength and frequency respectively for the longitudinal waves. There are other elastic moduli which describe other types of elastic deformation, and in MRE we actually measure the shear modulus. This describes the tissue stiffness when force is applied parallel to one of its surfaces, while the

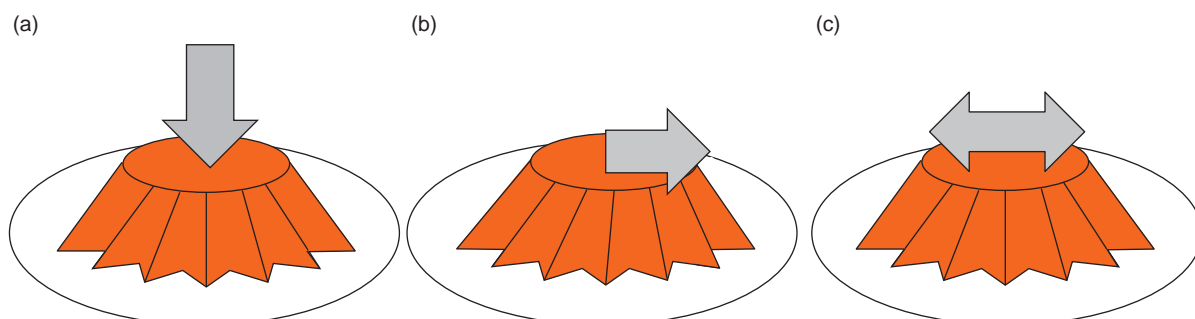


**Figure 19.13** Young's modulus of a jelly: (a) push down on the top. (b) Shear modulus of the jelly: pull the top surface to one side. (c) Shear waves in a jelly.

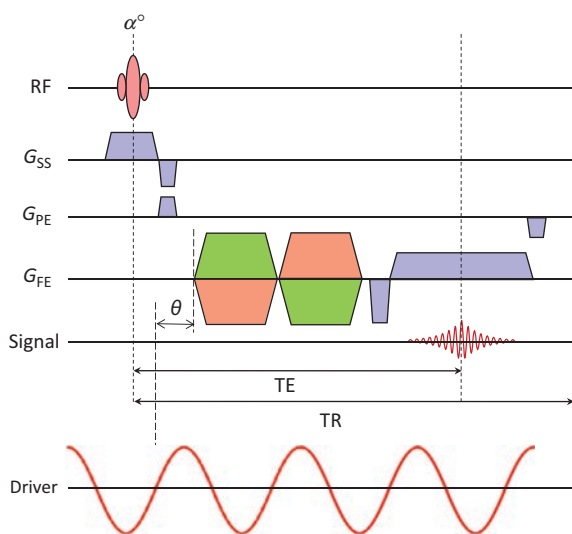


**Figure 19.14** Gradient-echo-based MRE sequence showing the bipolar motion encoding gradients (MEGs) in red and green for the two polarities. The driver waveform and its temporal relationship with the MEG is given by  $\theta$ .

opposite surface remains static. If you think about a jelly on a plate, you can measure  $E$  by pressing down on the top of the jelly (Figure 19.13a); to measure the shear modulus you need to pull the top surface of the jelly to one side (Figure 19.13b).

Like Young's modulus, the shear modulus  $\mu$  can be measured using a static deformation, or by setting up shear waves in the medium and again measuring the speed or wavelength of the waves:

$$c = \sqrt{\frac{\mu}{\rho}} \Rightarrow \mu = \frac{(\lambda f)^2}{\rho}$$

where again  $\rho$  is the mechanical density of the tissue, and now  $\mu$  is the shear modulus (not the magnetic moment of the proton, or the average of a set of

measurements). To set up shear waves in the jelly, you need to wobble the top surface of the jelly back and forth (Figure 19.13c) – or pick up the plate and shake it horizontally!

The MRE pulse sequence is essentially a variant of phase contrast velocity imaging: refer back to Section 15.3.2 for a refresher course. A pair of bipolar gradients is inserted in the pulse sequence, known as Motion Encoding Gradients (MEGs, Figure 19.14). The external driver creates mechanical vibrations in the body, and the MEGs encode the tiny tissue displacements as the phase of the MR signal. Since the displacements are truly tiny, typically  $10^{-7}$  mm, the MEGs are applied at the same frequency as the mechanical wave driver and with a controlled phase relationship  $\theta$ . The gradient limits of typical MR systems means that the MRE sequence is 'tuned' to a frequency which matches shear waves in tissue; longitudinal waves travel much faster and are 'invisible' with our current technology. Just as with PC angio, the MEGs are applied twice with opposite polarities, and the signal phases are subtracted to remove non-motion-related background phase shifts.

In order to calculate the tissue stiffness, we need to measure the speed of the shear wave propagation through the tissue. This can be done by repeating the acquisition but changing the phase offset ( $\theta$ ) between the driving waveform and the MEGs. Typically, four phase offsets are acquired, spaced equally over a period of the wave motion. If these four images are displayed as a movie, it gives an impression of the wave propagation through the tissue.

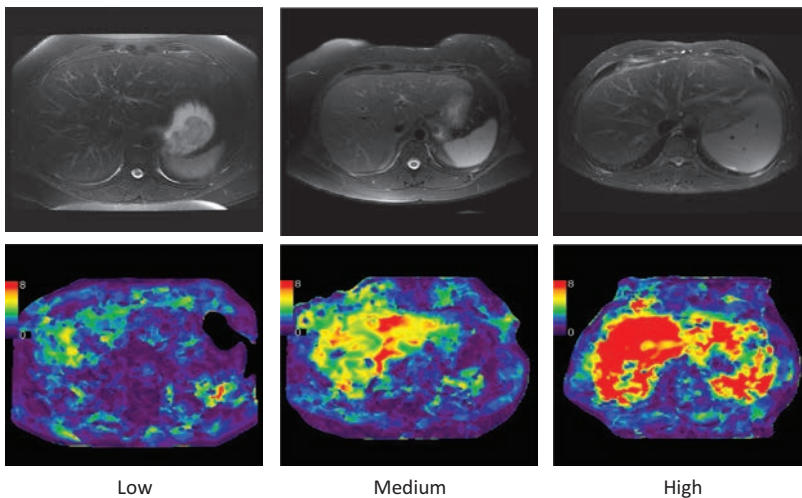


**Figure 19.15**  $T_2w$  images (top row) and MR elastograms (bottom row) in three patients with low (normal), medium and high liver stiffness. The elastograms are in the range 0–8 kPa. Note that there are no noticeable differences in the  $T_2w$  images, but the elastograms show clear differences in liver stiffness.

Remembering that the shear modulus is found from the relationship  $(\lambda f)^2/\rho$ , we assume  $\rho$  is  $1000 \text{ kg m}^{-3}$  and we know  $f$ , the operating frequency of the driver unit. We just need to determine  $\lambda$  from the wave images, something which turns out to be rather difficult, but possible if we use a number of simplifying assumptions. Following the MRE acquisition, an MR elastogram is produced (Figure 19.15).

In theory, MEGs can be used with several conventional MRI pulse sequences; however, for the clinical application of liver imaging it needs to be fast – achievable in a breath-hold. Typical commercial protocols are gradient echoes, with a limited number of slices and rather low spatial resolution matched to the driving frequency of the MRE device. Each phase offset  $\theta$  is acquired in a separate 15 s breath-hold acquisition. The liver MRE images shown here were acquired using a pneumatic driver at a frequency of 60 Hz. The driver is essentially an acoustic speaker positioned outside the magnet room, with an alternating current at the driver frequency applied to the speaker magnets. This causes the cone to oscillate, creating variations in air pressure. A length of plastic tubing transmits this pressure variation into the magnet room and ends with a small circular drum-like paddle which is positioned in close contact with the patient's abdomen, just overlying the liver. The surface of the drum vibrates, creating the mechanical waves that propagate through the tissue. Although the driver is sending longitudinal waves into the body, the internal boundaries (diaphragm, ribs, etc.) convert them into a mixture of longitudinal and shear waves.

While not painful, it is certainly a weird experience, particularly the first time!

#### Clinical Applications of MRE

MRE has primarily been used to quantify liver stiffness as a marker of hepatic disease progression. A number of studies have shown good correlations of mean liver stiffness with histopathological assessment of tissue obtained from liver biopsy. Hepatic disease characterization is currently the only commercially available application. However, researchers are exploring other clinical applications, e.g. the breast, where tumours are known to be stiffer than benign lesions; and the brain, where tissue stiffness may help in neurodegenerative diseases as well as brain cancers. New applications may need different mechanical devices to induce shear waves, and areas like the brain can be particularly difficult because the skull strongly attenuates the waves.

### 19.7 Accuracy, Precision, and Diagnostic Confidence

The move towards more quantitative MR methods is valuable for the whole community, as it improves objectivity and supports evidence-based medical decisions. Of course it is critical to know more about the measurement methods in order for them to reach widespread adoption, in particular accuracy and precision. This section will provide a short introduction to medical statistics; see Further reading at the end of the chapter for more detailed explanations.

Suppose we have a tissue sample which has a true  $T_1$  of 446 ms, measured by some gold standard technique. Now we make a  $T_1$  measurement using one of the methods described in Section 19.2.1: we hope that the result will match, but you will not be surprised if it is not exactly the same. If we make many measurements in the sample, we can find the accuracy of the technique: how close its results are to the true value provided by the gold standard method. We can also define the precision of the technique: sometimes called the test-retest reliability or repeatability.

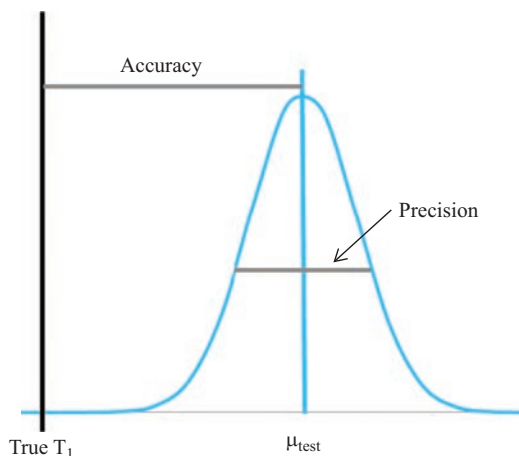


**Figure 19.16** Accuracy and precision.

Mathematically, the accuracy or *bias* is given as the difference between the mean of the sample measurements, 435 ms in our experiment, and the true value:  $\mu_{\text{test}} - T_{1,\text{true}}$ . (Note that  $\mu$  in this section is used for the mean or average of the set of measurements – not the magnetic moment of the proton, nor the shear modulus. Sorry for any confusion!) The precision is usually measured by finding the standard deviation of the sample measurements, assuming there is a Gaussian distribution of measurements about the mean:  $\sigma_{\text{test}} = 16$  ms in our experiment. Precision can also be described using the 95% confidence limits. Once again assuming a Gaussian distribution, the 95% confidence limits are at  $\mu_{\text{test}} \pm 1.96 \times \sigma_{\text{test}}$ , e.g. taking the data shown in Figure 19.16 the 95% confidence limits are 405 ms and 467 ms.

Suppose we now extend our testing, and measure the  $T_1$ s in a series of healthy subjects and in a group of patients with a particular disease. We assume that both groups have Gaussian distributions, so we can define the mean and standard deviation of  $T_1$  in each group. If the  $T_1$ s are well separated (Figure 19.17), we can have high confidence that a  $T_1$  measurement in a single subject will be able to distinguish between healthy and diseased tissue. We generally use Student's *t*-test to test the separation of the two results:

$$t = \frac{\mu_1 - \mu_2}{\sqrt{(\sigma_1^2/n_1) + (\sigma_2^2/n_2)}}$$

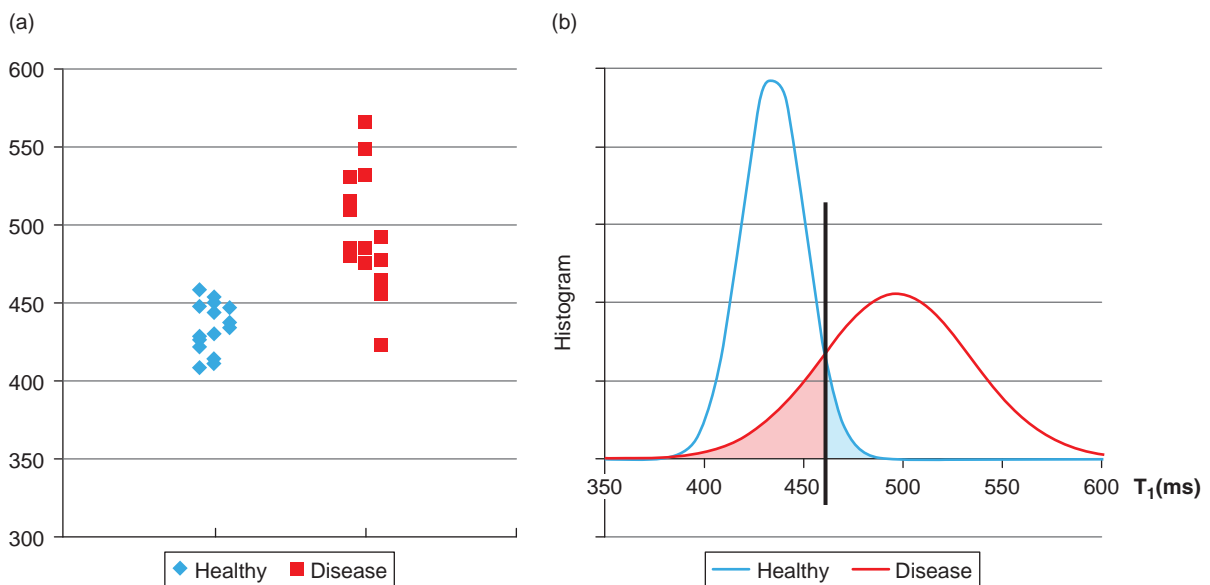


**Figure 19.17** (a) Hypothetical  $T_1$  results for healthy subjects and patients with a disease. (b) Histogram of results, showing the cut-off  $T_1$  to distinguish healthy and disease groups. Blue shaded area = false positive results, red shaded area = false negative results.

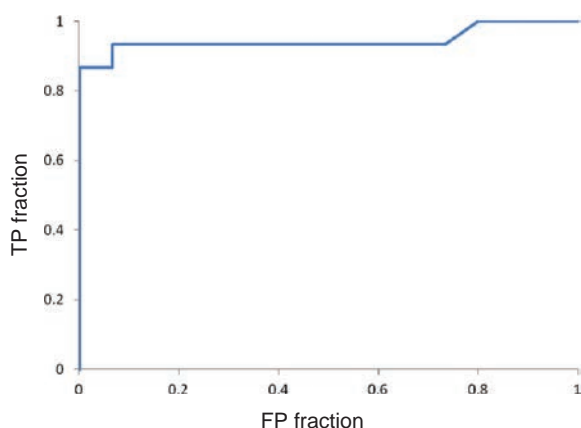


**Figure 19.18** ROC (receiver operating characteristic) curve for our hypothetical  $T_1$  experiment.

Statistics software can convert the resulting  $t$ -score into a probability  $p$ , which tells us the probability that the two samples are actually measuring the same thing (the null hypothesis). The smaller the  $p$ -value, the higher our confidence in the  $T_1$  measurement as a quantitative tool. Many research papers use thresholds of  $p < 0.05$  (5%),  $p < 0.001$  (0.1%), etc. to describe *significant differences* between the two sample groups. You can translate this as ‘there is only  $N\%$  probability that our experiment is showing separation of the means when it should show them overlapping’. In our example,  $p < 0.00001$ , a result which can be considered extremely promising – it shows that  $T_1$  measurement can easily distinguish between healthy and disease groups.

However, we need to take this one step further if we want to consider using our  $T_1$  technique to make a clinical decision in a single patient. You can see from Figure 19.17 that if we have overlapping distributions for normal and disease, we are going to have trouble if a patient’s result lands in the overlap region. As well as true positive (TP) and true negative (TN) results, there would be some false positive (FP) and false negative (FN) results. We can define two new metrics for our set of results: sensitivity and specificity.

$$\text{Sensitivity} = \frac{\text{TP}}{\text{TP} + \text{FN}}$$

$$\text{Specificity} = \frac{\text{TN}}{\text{TN} + \text{FP}}$$

In our example with a threshold of 460 ms, sensitivity = 0.86, and specificity = 1.00. Notice that if we change the threshold for  $T_1$ , we will also change the sensitivity and specificity. This can be mapped as an ROC (receiver operating characteristic) curve, as shown in Figure 19.18.

Finally, if the disease prevalence (Prev) is known, we can calculate the positive and negative predictive value of the test. The prevalence has to be estimated from population studies, not from our small sample experiment. The predictive values are found as follows:

$$\text{PPV} = \frac{\text{Sens} \cdot \text{Prev}}{\text{Sens} \cdot \text{Prev} + (1 - \text{Spec}) \cdot (1 - \text{Prev})}$$

$$\text{NPV} = \frac{\text{Spec} \cdot (1 - \text{Prev})}{\text{Spec} \cdot (1 - \text{Prev}) + (1 - \text{Sens}) \cdot \text{Prev}}$$

Using our  $T_1$  example again, if the disease has a prevalence of 1% in the general population, we have PPV = 12.3% and NPV = 99.9%. In words, this suggests that around 12% of patients who have a positive result from the  $T_1$  measurement actually have the disease; on the other side, nearly all the negative results are true negatives. Once again, the PPV and NPV are dependent on the choice of threshold to distinguish between healthy and disease.

As you can see from this brief introduction, quantitative MR is only the first step towards a truly useful diagnostic test, and you should be wary of results which only show the means of two groups. Our advice: always challenge yourself to measure the confidence intervals or sensitivity and specificity to get a better idea of the potential diagnostic value of your exciting new method!

#### See also:

- Fat suppression techniques: Section 7.3

## Further Reading

Bernstein MA, King KF and Zhou XJ (2004) *Handbook of MRI Pulse Sequences*. London: Elsevier Academic Press, chapter 17.

Bland M (2000) *An Introduction to Medical Statistics*, 3rd edition. Oxford: Oxford University Press.

Crema MD, Roemer FW, Marra MD, et al. (2011) ‘Articular cartilage in the knee: current MR imaging

techniques and applications in clinical practice and research’. *RadioGraphics*, 31:37–61. Available online at <http://pubs.rsna.org/toc/radiographics/31/1> [accessed 1 April 2015].



- Delfaut EM, Beltran J, Johnson G, Rousseau J, Marchandise X and Cotten A. (1999) 'Fat suppression in MR imaging: techniques and pitfalls'. *RadioGraphics* 19:373–382.
- Deoni SCL, Rutt BK and Peters TM (2003) 'Rapid combined  $T_1$  and  $T_2$  mapping using gradient recalled acquisition in the steady state'. *Magn Reson Med* 49:515–526.
- Eggers H and Börnert P (2014) 'Chemical shift encoding-based water–fat separation methods'. *J Magn Reson Imaging* 40:251–268.
- Leenders KL, Perani D, Lammertsma AA, *et al.* (1990) 'Cerebral blood flow, blood volume and oxygen utilisation: normal values and effect of age'. *Brain* 113:27–47.
- Thomas Dixon WT (1984) 'Simple proton spectroscopic imaging'. *Radiology* 153: 189–194.
- Wood JC, Enriquez C, Ghurgr N, *et al.* (2005) 'MRI  $R_2$  and  $R_2^*$  mapping accurately estimates hepatic iron concentration in transfusion-dependent thalassaemia and sickle cell disease patients'. *Blood* 106:1460–1465.